



CHORUS

This is the accepted manuscript made available via CHORUS. The article has been published as:

Characterization of dot-specific and tunable effective g factors in a GaAs/AlGaAs double quantum dot single-hole device

A. Padawer-Blatt, J. Ducatel, M. Korkusinski, A. Bogan, L. Gaudreau, P. Zawadzki, D. G. Austing, A. S. Sachrajda, S. Studenikin, L. Tracy, J. Reno, and T. Hargett

Phys. Rev. B **105**, 195305 — Published 11 May 2022

DOI: [10.1103/PhysRevB.105.195305](https://doi.org/10.1103/PhysRevB.105.195305)

Characterisation of dot-specific and tunable effective g-factors in a GaAs/AlGaAs double quantum dot single-hole device

A. Padawer-Blatt and J. Ducatel

*Emerging Technologies Division, National Research Council of Canada, Ottawa, ON, K1A0R6, Canada and
Department of Physics and Astronomy, University of Waterloo, Waterloo, Ontario N2L 3G1, Canada*

M. Korkusinski, A. Bogan, L. Gaudreau, P. Zawadzki, D. G. Austing, A. S. Sachrajda, and S. Studenikin*
Emerging Technologies Division, National Research Council of Canada, Ottawa, ON, K1A0R6, Canada

L. Tracy

Sandia National Laboratories, Albuquerque, NM, 87185, USA

J. Reno and T. Hargett

Center for Integrated Nanotechnologies, Sandia National Laboratories, Albuquerque, NM, 87185, USA

(Dated: April 13, 2022)

Difference in g-factors in multi-dot structures can form the basis of dot selective spin manipulation under global micro-wave irradiation. Employing electric dipole spin resonance facilitated by strong spin-orbit interaction (SOI), we observe differences in the extracted values of the single-hole effective g-factors of the constituent quantum dots of a GaAs/AlGaAs double quantum dot device at the level of $\sim 5\text{-}10\%$. We examine the continuous change in the hole g-factor with electrical detuning over a wide range of inter-dot tunnel couplings and for different out-of-plane magnetic fields. The observed tendency of the quantum dot effective g-factors to steadily increase on decreasing the inter-dot coupling or on increasing the magnetic field is attributed to the impact on the SOI of changing the dot confinement potential and heavy-hole light-hole mixing.

Confined holes in semiconductor quantum dot systems are attracting a rapidly growing interest due to several appealing properties. The properties include: strong spin-orbit interaction (SOI) desirable for fast and convenient all-electric spin manipulation; highly anisotropic and tunable hole g-factors; and in group III-V semiconductors where interaction with the spins of the host material nuclei cannot be avoided, the coupling of the hole spins to the nuclei is significantly reduced compared to electron spins. See our recent topical review in Ref. [1] and references therein. The attraction of efficient control through strong SOI of spin qubits, particularly those featuring holes, and details of the mechanisms are discussed elsewhere [2–6]. In our recent work focusing on single holes confined in lateral quantum dots (QDs) in the GaAs/AlGaAs material platform, we have shown strong SOI introduces efficient spin-flip inter-dot tunneling channels [7], and leads to a strong voltage tunable spin-gap renormalization [8]. A consequence of both is an electrically tunable effective g-factor, g_{eff} , that is different from the familiar effective g-factor, g^* , taken to be a constant determined solely by material properties. Taking advantage of the strong SOI offered by holes in semiconductors to couple electrically their spin and spatial motion through micro-wave (MW) signals applied to gates, the technique of electric-dipole spin resonance (EDSR) [9, 10] is not only a powerful tool to gain insight into the physics underlying g_{eff} but can also drive

spin rotations efficiently [11–13]. See Ref. [1] for a comprehensive review of recent work on EDSR with holes in QD systems and in semiconductor materials other than the GaAs/AlGaAs system, along with an overview of the physics underlying the principal EDSR mechanisms exploiting SOI.

In Ref. [8], employing EDSR in conjunction with strong SOI in the GaAs valence band, we demonstrated the electrical tunability of the effective g-factor of a single-hole spin confined in a lateral GaAs/AlGaAs double quantum dot (DQD) device. In that work, we considered only the case of the strong inter-dot coupling regime (spin conserving tunneling matrix element $\sim 100 \mu\text{eV}$ for a magnetic field approaching zero), and applied a model to fit the experimental data assuming the g-factors in both QDs are identical. Here, we extend our application of the EDSR technique for single holes to cover the impact of tuning the inter-dot coupling over a wide range down to the weak inter-dot coupling regime, and adapt our model to account for small differences in QD g-factors inevitably present. As discussed elsewhere, the holes confined in the DQD relevant to our discussion here for planar GaAs/AlGaAs structures are predominantly heavy-hole in character [1, 14]. As will become clear in the following discussion, we will take strong, intermediate, and weak inter-dot coupling, SC, IC, and WC, respectively to be many tens, a couple tens, and a few micro-electron volts.

Figure 1(a) shows a scanning electron micrograph of the lateral DQD device. Full details of the undoped GaAs/Al_{0.5}Ga_{0.5}As hetero-structure and device fabrication are given in Refs. [7, 8, 14–17]. Holes are accumu-

* Author to whom correspondence should be addressed: sergei.studenikin@nrc-cnrc.gc.ca

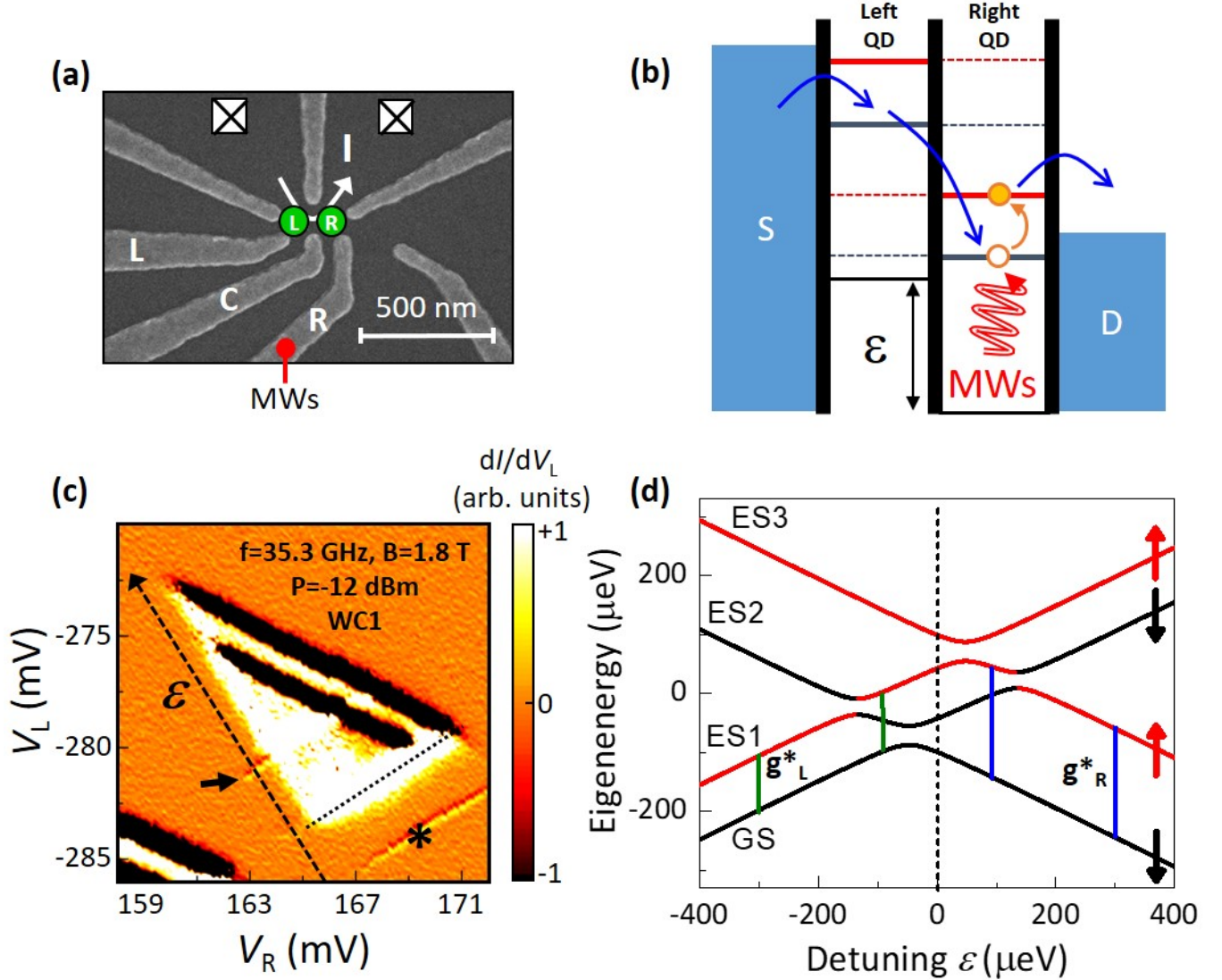


FIG. 1. (a) Scanning electron micrograph of DQD device. A global top gate on an insulating material is also present (not shown). Voltages V_L and V_R respectively on the left (L) and right (R) plunger gates regulate the number of holes on the left and right QDs. Voltage V_C on the center (C) gate controls the inter-dot coupling. The crossed boxes represent Ohmic contacts. Current, I , flows through the DQD in response to an applied source-drain bias, V_{SD} . Micro-waves (MWs) are applied to the right plunger gate. Scale bar: 500 nm. (b) Schematic showing quantum molecular levels when system is in an energy blocked condition in the absence of MWs. MW modulation is shown as exciting a spin-down hole trapped predominantly on the right QD onto the first excited state, spin-up also predominantly on the right QD, from where the hole can exit to the drain (D). (c) Single-hole high-bias transport triangle for weak inter-dot coupling (condition WC1) at $B = 1.8$ T with MWs applied at frequency $f = 35.3$ GHz and power $P = -12$ dBm. dI/dV_L , in arbitrary units, is plotted as a function of V_L and V_R , and $V_{SD} = -0.5$ mV which corresponds to holes flowing from left to right in panel (b). The dotted line identifies the base of the bias triangle. The black arrow (asterisk) marks the EDSR signal for positive (negative) detuning ϵ . In subsequent measurements V_L and V_R are simultaneously scanned so as to sweep ϵ and cut through the EDSR features outside of the bias triangle - see dashed arrow for example. (d) Calculated eigenenergies as a function of detuning for model parameters $B = 2.0$ T, $t_N = 16.7$ μeV , $t_F = 13.0$ μeV , $g_L^* = 0.8$, and $g_R^* = 1.6$. GS, ES1, ES2, ES3, and ES4 correspond respectively to the ground and first three excited states. Black (red) identifies spin-down (spin-up). Green (blue) vertical lines identify examples of predominantly spin-excitations in the left (right) QD. In the vicinity of the ES1-ES2 anti-crossings the spin is hybrid spin-up and spin-down, and transitions from GS are hybrid spin-charge transitions. *We stress that for illustration we have grossly exaggerated the difference in g -factor between the two dots. The actual difference is typically 5-10%. Note in panels (b) and (d), and hence forth in this article, for convenience, the positive direction of the energy axis corresponds to increasing hole energies.*

lated at the hetero-interface by a global gate. Voltages V_L and V_R respectively on the left (L) and right (R) plunger gates are used to tune the hole confining potentials in each QD, while voltage V_C on the center (C) gate is used to adjust the inter-dot coupling. Current, I , flows through the two coupled QDs when a source-drain bias, V_{SD} , is applied. Measurements are performed in a dilution refrigerator and the effective hole temperature is ~ 100 mK. A magnetic (B-) field is applied out-of-plane. MWs are applied to the right plunger gate. The MW power P quoted throughout this article is the nominal MW power at the MW source. The MW signal is attenuated by -20 dB at the 1 K stage and is further reduced by frequency-dependent loss in the coaxial lines [8]. As we report extensively elsewhere, verified by both transport and charge detection measurements, we are able to reach the single-hole regime [1, 8, 14].

We established in Ref. [8] that EDSR features arise on MW excitation in the vicinity of the single-hole high-bias transport triangle. Figure 1(b) depicts the origin of one of the EDSR features for the situation where, in the absence of MWs, one hole is trapped on the right QD (energy blockaded) and no current can flow. MW modulation at the appropriate frequency can promote the spin-down hole occupying the ground molecular state with weight largely on the right QD onto the first excited molecular state, spin-up also weighted largely on the right QD, from where the hole can exit to the drain (D). Note the schematic is drawn for the case where the dot g-factors are taken to be equal.

Figure 1(c) shows an example of a single-hole high-bias transport triangle for a weak inter-dot coupling condition (WC1: see discussion later regarding coupling conditions and the labelling thereof) at $B = 1.8$ T with MWs applied at frequency $f=35.3$ GHz and power $P=-12$ dBm (see also Supplemental Fig. S1 which includes charge boundaries and hole occupation numbers [18]). Here $V_{SD} = -0.5$ mV: negative bias polarity corresponds to holes flowing from left to right in panel (b). Two resonant transition lines located outside the bias triangle are clearly identified. The black arrow points to the EDSR signal for positive detuning ε : hole initially trapped on the right QD [case depicted in Fig. 1(b)], i.e., the right QD hole spin-down energy level is lower than the left QD hole spin-down energy level. The asterisk marks the EDSR signal for negative detuning ε [8]: hole initially trapped on the left QD, i.e., the left QD hole spin-down energy level is lower than the right QD hole spin-down energy level. These two features are approximately equidistant from and parallel to the base of the bias triangle (dotted line). Also, they are of comparable strength. Although the MW modulation is applied to the right plunger gate, both QDs see the MWs. Therefore conditional on the weight of the occupancy of the single hole trapped on the left or right QD, an excitation is possible in either QD if the MW frequency matches an energy gap between levels.

In Refs. [1, 8] it was assumed in the modelling of

the EDSR data taken in the strong inter-dot coupling regime that the g-factors of the two QDs are equal. The schematic in Fig. 1(b) is also drawn for this situation. The key finding of our work here is that the EDSR technique is sufficiently sensitive to detect small differences in the dot g-factors. For illustration of what we can expect when the g-factors of the two QDs are not equal consider the following. Figure 1(d) shows the calculated eigenenergies of the ground state (GS) and the first three excited states (ES1, ES2, ES3) as a function of detuning for model parameters $B = 2.0$ T, $t_N = 16.7$ μeV , $t_F = 13.0$ μeV , $g_L^* = 0.8$, and $g_R^* = 1.6$. t_N , t_F , g_L^* , g_R^* respectively are the spin-conserving tunneling matrix element, spin-flip tunneling matrix element accounting for the spin-orbit interaction, effective g-factor of the left QD, and effective g-factor of the right QD. We have straightforwardly modified the model described in Refs. [1, 8] to account for different Zeeman splitting energies in the left and right QDs. Henceforth we refer to this model as the two g-factor model. For the lowest energy excitation corresponding to the GS \rightarrow ES1 transition, we expect that at large negative (positive) detuning the transition tends to an energy, independent of detuning, reflecting the value of g_L^* (g_R^*): see green (blue) vertical lines near -300 μeV (+300 μeV) in detuning showing an excitation in the left (right) QD that is principally spin-like in character. For detuning in the range of -135 μeV to +135 μeV the GS \rightarrow ES1 transition becomes strongly detuning dependent and is charge-like in character. The minimum energy reflects the strength of spin-conserving tunneling. For the next higher energy excitation corresponding to the GS \rightarrow ES2 transition, we expect that at large negative and positive detuning the transition is linear in detuning, and is charge-like in character. The dependence for detuning in the range of -135 μeV to +135 μeV is quite different. For detuning between -135 μeV and -45 μeV (+45 μeV and +135 μeV) the excitation energy is nearly constant reflecting the value of g_L^* (g_R^*): see green (blue) vertical lines near -90 μeV (+90 μeV) in detuning showing excitations in the left (right) QD that are spin-like in character. A smooth evolution in the excitation energy occurs for detuning between -45 μeV and +45 μeV . This step-like change in the GS \rightarrow ES2 transition at small detuning between two excitation energies reflective of a difference in g_L^* and g_R^* is expected to become more pronounced as the inter-dot coupling strength is progressively reduced (see Fig. 3 and discussion later). We note that for clear illustration here we have grossly exaggerated the difference in g-factor between the two QDs. As we will soon demonstrate, in actuality, the difference between the two QD g-factors is much smaller, at the level of 5-10%. We note that in our model zero detuning corresponds to the crossing of the lowest energy single-hole levels in the left and right QDs at zero B-field and in the absence of tunnel coupling. Consequently, for our choice of very different left and right QD g-factors, the maximum in the GS energy in Fig. 1(d) is noticeably shifted to negative detuning

at finite B-field. For smaller realistic differences in the g-factor this maximum, also marking the onset of transport at the base of the bias triangle, occurs at $\varepsilon \approx 0$.

Figure 2(a) shows the frequency dependence of the measured EDSR signal as a function of detuning for an intermediate inter-dot coupling condition (IC1) at $B = 2$ T and $V_{SD} = +1$ mV. Two branches corresponding to the GS \rightarrow ES1 and GS \rightarrow ES2 MW transitions are clear. The sweep in detuning is generated by simultaneously changing V_L and V_R in such a way as to cut through the EDSR features outside of the bias triangle [see dashed arrow, for example, in the case of bias triangle for the SC condition in Fig. 1(c)]. From such data we can extract the position of the EDSR peaks. Since we are interested in the EDSR peak position and not the EDSR peak height, details of the tunneling rates for the barriers to the source and drains contacts are not important here [19].

Figures 2(b)-(d) show the extracted peaks position as a function of detuning for strong (SC), intermediate (IC1), and weak (WC1) coupling conditions at 2 T. For SC case, only the GS \rightarrow ES1 transition is recorded, whereas for IC1 and WC1 cases, the GS \rightarrow ES2 transition is additionally observed. The upper bound for the MW frequency we can apply is 50 GHz limited by the MW source. To track the EDSR over a wide range of frequency, because MW losses in the coaxial lines grow with increasing MW frequency, the data is often captured in blocks for which the MW power is progressively stepped-up to compensate. The data blocks are then stitched together. The magnitude and sign of the applied bias voltage also determines the accessible detuning range. For sufficiently large bias, the single-hole transport triangle will merge with the adjoining transport triangle. Also there tends to be more extractable data points at negative (positive) detuning for an applied positive (negative) bias voltage. In the three panels, the dashed lines are fits to the EDSR peaks according to the two g-factor model. The fitted values for g_L^* and g_R^* are also given. Although we can calibrate the energy scale on the detuning axes from details of the DQD transport characteristics on changing V_L and V_R , since the onset of transport along the base of the transport triangle is not generally sharp, it is not always straightforward to determine zero detuning precisely, even for the case of $g_L^* = g_R^*$, hence we have manually shifted the detuning axis scales in the Fig. 2 panels by small amounts so that the minimum in frequency for the GS \rightarrow ES1 transition is set to be at $\varepsilon = 0$: this applies too for the data shown in Fig. 3. We note here that the data shown in both Fig. 2 and Fig. 3, and the determination of coupling parameters, for example, as discussed below, does not rely solely on EDSR where the transition is predominantly spin-like, but also on photon-assisted tunneling when the transition is predominantly charge-like: see Ref. [8] for further discussion.

As the inter-dot coupling (t_N) is reduced from strong coupling to weak coupling several trends are immediately clear in Figs. 2(b)-(d). First, the zero-detuning mini-

mum frequency for the GS \rightarrow ES1 transitions decreases. The minimum frequency generally reflects directly the strength of the spin-conserving tunneling. Values for t_N determined from the fits for SC, IC1, and WC1 data sets respectively at 2 T are 63, 28, and 6 μeV - the error in these values is at the $\sim \pm 1$ μeV level. For IC1 and WC1 cases, the minimum frequency is essentially given by $\sim 2t_N$. Our classification of strength of inter-dot coupling now becomes clear. We generally declare strong, intermediate, and weak inter-dot coupling respectively to be many tens, a couple tens, and a few micro-electron volts (see also discussion related to Fig. 4). Second, the anti-crossing gap between GS \rightarrow ES1 and GS \rightarrow ES2 branches at finite detuning is larger for IC case than WC1 case. The anti-crossing gap here arises from spin-flip tunneling facilitated by the strong spin-orbit interaction and is quantified by the spin-flip tunneling matrix element t_F . For SC case, the GS \rightarrow ES2 branch is out of range for this set of data, but the comparatively weak curvature in the GS \rightarrow ES1 branch at finite detuning as the frequency starts to flatten points to a significant spin-flip contribution. Values of t_F determined from the fits for SC, IC1, and WC1 data sets respectively at 2 T are 41, 16, and 6 μeV . As discussed in Refs. [1, 7, 8] t_F is comparable in value to t_N and dependent to a degree on t_N so the decrease in t_F with reduced inter-dot coupling is expected. Third, the range over which the effective g-factor g_{eff} associated with the GS \rightarrow ES1 branch can be tuned by changing the detuning at fixed B-field, here 2 T, clearly grows as the tunnel coupling weakens (the right axis scale in each panel directly gives g_{eff}). This broad tunability in g_{eff} with static electric fields is attractive for potential qubit manipulations with global MW illumination: see Refs. [1, 8] for extended commentary. Lastly, not only do the fits reveal that g_L^* and g_R^* are different at the level of 5-10% with $g_L^* < g_R^*$, which is useful for local manipulations, but both g_L^* and g_R^* steadily increase as the inter-dot coupling decreases - for the sequence shown the changes in g-factor is 15-20%. The small difference in the QD g-factors is not unexpected. Statistical variations in dot g-factors in multi-dot devices of magnitude 1-10% due to microscopic differences in the dot environment, for example, due to variation in the local confinement from disorder, are documented [20-23]. We note these works applied the EDSR technique to GaAs/AlGaAs hetero-structure QD circuits confining single electrons. See also Refs. [12, 24] featuring Ge/SiGe hetero-structure QD circuits confining multiple holes whereby the difference in hole g-factors between the QDs is ascribed to different QD sizes and hole occupancies, i.e., orbital effects. We comment further on the steady increase in g_L^* and g_R^* on decreasing the inter-dot coupling later when we discuss Fig. 4(b).

Also becoming apparent in the WC1 data in Fig. 2(d) is the near flat dependence of the GS \rightarrow ES2 transition frequency for detuning in the range of -150 to 150 μeV other than a small step near zero detuning reflecting the change in g_{eff} from 1.33 to 1.39. The step-like behaviour

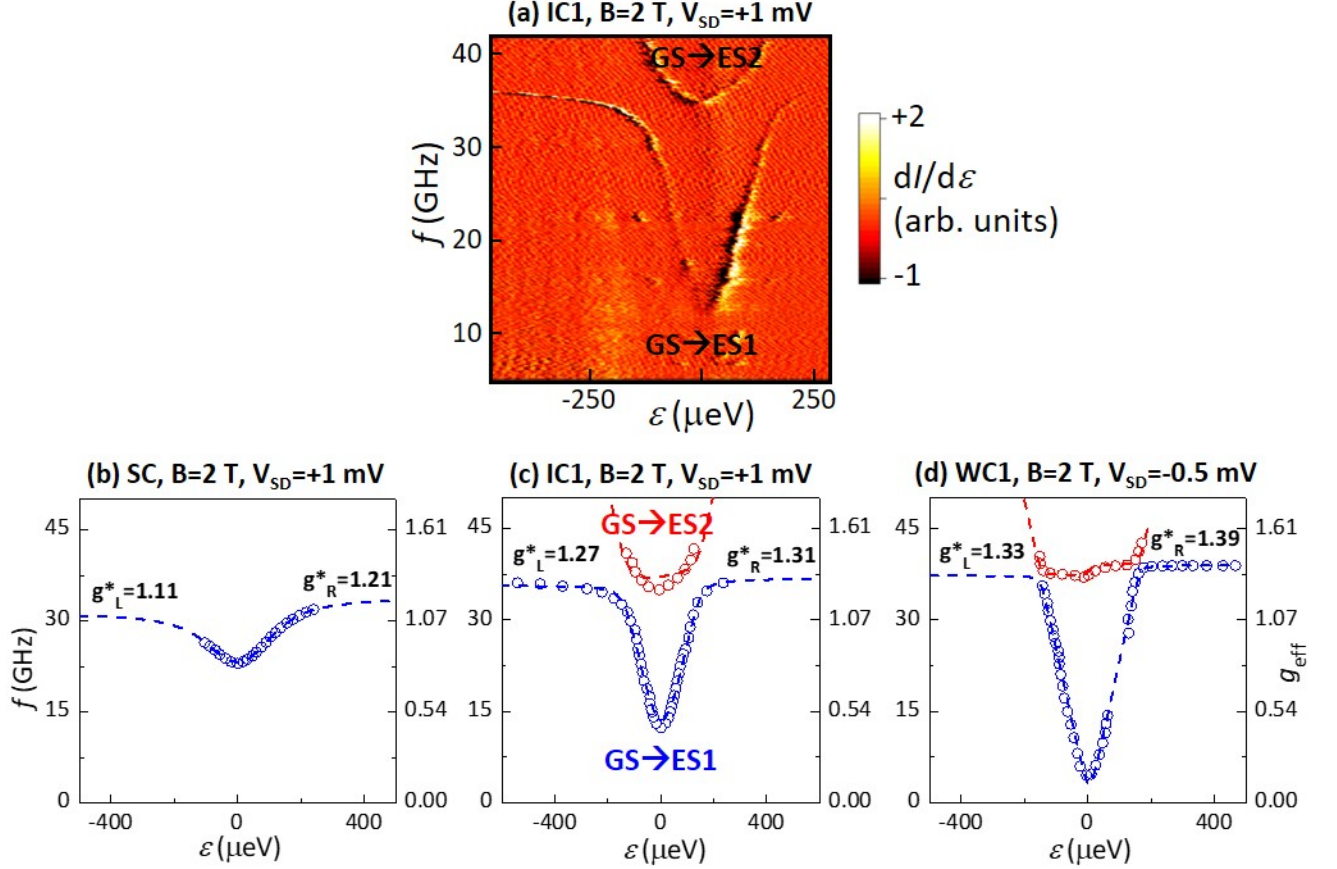


FIG. 2. (a) Frequency f dependence of the measured EDSR signal in $dI/d\varepsilon$ (arbitrary units) as a function of detuning ε for intermediate inter-dot coupling (condition IC1) at $B = 2.0$ T and $V_{SD} = +1$ mV. Two branches corresponding to the $\text{GS} \rightarrow \text{ES1}$ and $\text{GS} \rightarrow \text{ES2}$ MW excitations are visible. The plot is built up from three adjoining blocks of data captured consecutively: the MW power is stepped up from -20 to -15 dBm at $f = 15$ GHz and then finally to -6 dBm at $f = 22$ GHz. (b) Frequency dependence of extracted EDSR peak position as a function of detuning for strong inter-dot coupling (condition SC) at $B = 2.0$ T and $V_{SD} = +1$ mV. P is set to 0 dBm. Only points for the $\text{GS} \rightarrow \text{ES1}$ branch could be extracted (the $\text{GS} \rightarrow \text{ES2}$ branch is out of range). (c) Frequency dependence of EDSR peak position as a function of detuning for intermediate inter-dot coupling (condition IC1) extracted from the plot in panel (a). Data points for the $\text{GS} \rightarrow \text{ES1}$ ($\text{GS} \rightarrow \text{ES2}$) branch are colored blue (red). (d) Frequency dependence of extracted EDSR peak position as a function of detuning for weak inter-dot coupling (condition WC1) at $B = 2.0$ T and $V_{SD} = -0.5$ mV. P is set to -28 (-12) dBm below (above) 23 GHz. For panels (b)-(d), blue and red dashed lines are fits to the data according to the two g -factor model. The fitted values for g_L^* and g_R^* are also indicated, and for convenience, a right axis scale is included to show directly $g_{\text{eff}} = hf/\mu_B B$.

here is a signature of differing g -factors in the two QDs, consistent with our discussion above in connection to the calculated eigenenergies plot for model parameters in Fig. 1(d), and should become more apparent at weaker inter-dot coupling when the anti-crossing gap between $\text{GS} \rightarrow \text{ES1}$ and $\text{GS} \rightarrow \text{ES2}$ branches is diminished. Figure 3 emphasises the trend. Here we plot the frequency dependence of the extracted EDSR peak position as a function of detuning for three inter-dot coupling conditions: (a) IC2; (b) WC1; and (c) WC2. Of these three coupling conditions, IC2 (WC2) is the strongest (weakest). Note the coupling for IC2 is slightly less than that for IC1: t_N for IC1 (IC2) at 2 T (1.8 T) is $28 \mu\text{eV}$ ($24 \mu\text{eV}$). For panels (a) and (b), fits to the data according to the two g -factor model are included. For panel (c), a fit to the

data with the two g -factor model could not be reliably obtained due to a combination of insufficient data points below 25 GHz, especially near the frequency minimum in the $\text{GS} \rightarrow \text{ES1}$ transition at zero detuning, and insufficient data resolution in the vicinity of the now small anti-crossing gaps between $\text{GS} \rightarrow \text{ES1}$ and $\text{GS} \rightarrow \text{ES2}$ branches at finite detuning in the limit of very weak inter-dot coupling. The fitted [estimated] values for g_L^* and g_R^* in (a) and (b) [(c)] are also indicated. On inspection of the three data sets, clearly on decreasing the inter-dot coupling, as discussed above, the g_L^* and g_R^* increase, and the anti-crossing gap between $\text{GS} \rightarrow \text{ES1}$ and $\text{GS} \rightarrow \text{ES2}$ branches shrinks leading to a sharper step near $\varepsilon = 0$.

Lastly, we provide in Fig. 4 a compilation of the tunneling elements t_N and t_F [panel (a)], and the left QD

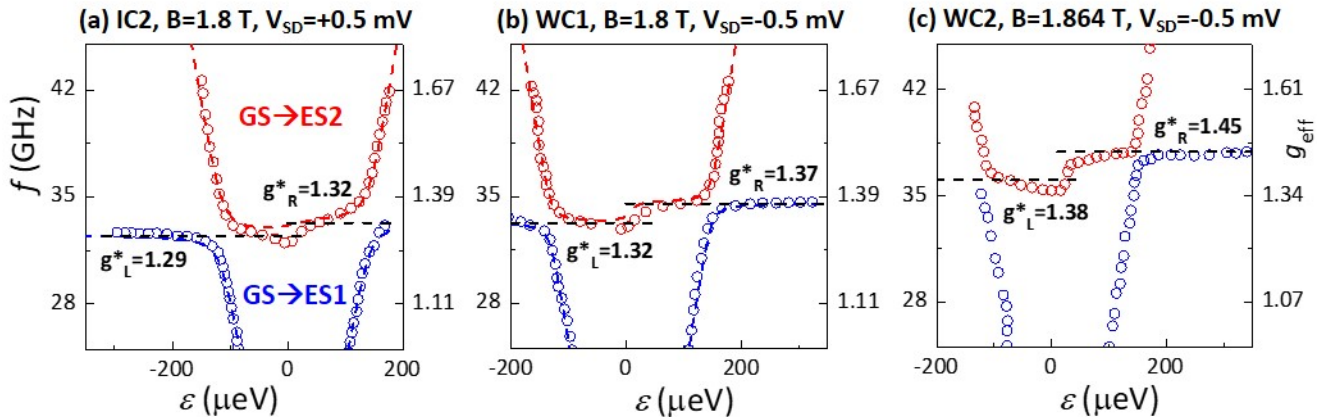


FIG. 3. Frequency dependence of extracted EDSR peak position as a function of detuning for inter-dot coupling conditions: (a) IC2 at $B = 1.8$ T and $V_{SD} = +0.5$ mV ($P = -12$ dBm); (b) WC1 at $B = 1.8$ T and $V_{SD} = -0.5$ mV ($P = -12$ dBm); and (c) WC2 at $B = 1.864$ T and $V + SD = -0.5$ mV ($P = -5$ dBm). Of these three coupling conditions, IC2 (WC2) is the strongest (weakest). Data points for the GS \rightarrow ES1 (GS \rightarrow ES2) branch are colored blue (red). For panels (a) and (b), blue and red dashed lines are fits to the data according to the two g-factor model. For panel (c), a fit to the data with the two g-factor model could not be reliably obtained. The fitted [estimated] values for g_L^* and g_R^* in (a) and (b) [(c)] are also indicated, and for convenience, a right axis scale is included to show directly g_{eff} .

g-factor g_L^* [panel (b)]. These parameters are extracted from the two g-factor model for strong (SC), intermediate (IC1), and weak (WC1) inter-dot coupling conditions as a function of magnetic field. Regarding the tunneling elements we make the following three observations. First, the motivation for our classification of strong, intermediate, and weak inter-dot coupling respectively as many tens, a couple tens, and a few micro-electron volts, particularly evident at low B-field (< 1 T), is clear. For all the coupling conditions considered in this article, the ordering from strongest to weakest coupling is SC, IC1, IC2, WC1, and WC2. Second, as comprehensively discussed in Refs. [1, 7, 8] t_N and t_F are of comparable magnitude, and the general decrease in their values with increasing B-field reflects the decreasing overlap between the left QD and the right QD orbitals driven by diamagnetic squeezing of the cyclotron orbits. Interestingly, the B-field dependence of t_N and t_F for the case of SC notably deviate strongly from each other with increasing B-field, whereas those in the case of IC1 and WC1 track each other closely. The reason for this difference is currently not understood. Third, the values of t_N and t_F for SC, here obtained from the two g-factor model, are a little different but quite comparable to those reported in Ref. [8] determined with a model assuming the g-factors in the two QDs are identical. Regarding the g-factors, as exemplified here by g_L^* (the trends are similar for g_R^* : see Supplemental Fig. S2 [18]), we make the following comments.

The propensity for the g^* to increase with B-field for a given coupling condition in Fig. 4(b), as well as for g^* to steadily increase on decreasing the inter-dot coupling at a given B-field as seen in Fig. 2 and Fig. 4, we attribute to a tuning of the microscopic nature of the hole states, and specifically to the reduction of the admixture

of the light-hole sub-bands. The degree of heavy-hole-light-hole mixing is sensitive to the energy separation between the sub-bands as well as to the magnitude of the momentum matrix element describing the sub-band mixing [3, 5, 25, 26]. As the B-field and the gate voltages are tuned, the degree of mixing is impacted by: changes in the dot confinement potential, both in the shape and the strength, brought about by the change in voltage V_C on the center gate aimed at reducing the inter-dot coupling, and increase in the B-field leading to the diamagnetic squeezing of orbitals. Both effects strengthen the hole confinement and change the symmetry of the hole wave functions. The alteration of the spin-orbit interaction by change of dot confinement has been reported for electrons [27, 28] and for holes [24]. See also Refs. [25, 26, 29] for discussion of the influence of the size, shape, and geometry of a self-assembled dot, tailored, for example, through the growth process [30], on the hole wave functions and subsequently hole mixing. As discussed in Refs. [1, 14], for the GaAs/AlGaAs hetero-interface employed, heavy-holes are strongly localized laterally by the potential imposed by the voltages applied to the gates, whereas the light-hole states are essentially delocalized in-plane. Further localization by reducing the inter-dot coupling or diamagnetically squeezing the QD orbitals tends to raise the energy of the heavy-hole (measured from the valence band edge) but not the light-hole states leading to a further reduction of the already weak heavy-hole-light-hole mixing [3, 5]. The net effect is the g-factor of the lowest energy sub-band should increase, as observed, as the sub-band becomes more heavy-hole-like. We emphasise that the g^* values shown in Fig. 4(b) and Fig. S2 [18] were determined in the asymptotic limit at large detuning as illustrated in Fig. 3 so are not impacted directly by t_N and t_F , i.e., at large detuning essentially the individual

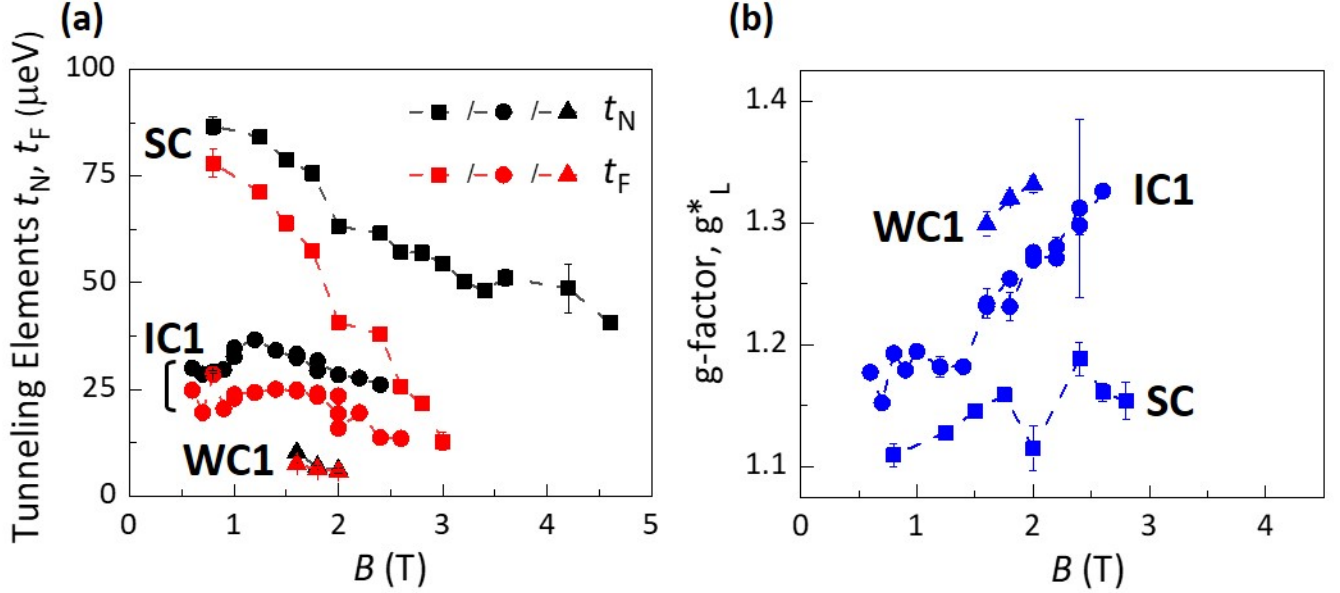


FIG. 4. Compilation of (a) tunneling elements t_N (black symbols) and t_F (red symbols), and (b) left QD g-factor g_L^* extracted from the two g-factor model for strong (SC: squares), intermediate (IC1: circles), and weak (WC1: triangles) inter-dot coupling conditions as a function of magnetic field. MW power and source-drain voltage conditions may differ for data points at a given inter-dot coupling condition. Also, for IC1, the compilations consists of overlapping data sets.

dots are probed rather than the coupled double dot.

In itself, the decrease of the inter-dot couplings with B-field [Fig. 4(a)] is not the direct driver for the increase of g^* -factors with B-field [Fig. 4(b) and Fig. S2], rather it is the impact of heavy-hole-light-hole mixing.

In itself, the decrease of the inter-dot couplings with B-field [Fig. 4(a)] is not the direct cause of the increase g^* with B-field [Fig. 4(b) and Fig. S2], rather it is the impact of the heavy-hole-light-hole mixing. We emphasise that all DQD gate voltages are changed in the process of tuning between the WC1-IC1-SC coupling regimes which affects both the tunneling matrix elements and the QD confining potentials (shape and strength).

In summary, utilizing the EDSR tool in the single-hole regime, we found the hole effective g-factors for the two QDs of a GaAs/AlGaAs DQD device differ by $\sim 5\text{-}10\%$. Additionally we demonstrated the hole g-factor can be varied over a wide range dependent not only on the electrical detuning, but also the inter-dot tunnel coupling, and the out-of-plane B-field. This tunability attests to the importance of the strong SOI in a two-dimensional system further influenced by change in the hole confinement, and mixing between heavy-hole and light-hole sub-bands. As an alternative to on-chip micro-magnets [31], constituent QDs in multi-dot structures with different g-factors furnish dot selective spin manipulations. Additionally electrical adjustment of the detuning to change the hole g-factor continuously and smoothly in a controlled manner to a desired value while the system is subject to global MW irradiation is convenient, and provides circuit functionality to switch between spin-like

and spin-charge-hybrid excitation regimes. The former (latter) regime is good when, for example, long spin relaxation and dephasing times for qubit operations are (coupling to a MW cavity for long-range qubit-qubit coupling is) required. These potential functionalities featuring holes are more extensively discussed in our work in Refs. [1, 8]: see also Refs. [32–38]. The means to control the hole g-factor described in this article add to those described in our earlier work whereby the heavy-hole g-factor can be set to nearly zero by applying an external B-field in-plane as opposed to out-of-plane [14, 39]. Hole effective g-factors that are electrically tunable through SOI are also reported in Refs. [12, 24] for planar Ge/SiGe QD circuits in the multi-hole regime. In Ref. [24], although individual QD g-factors are not determined directly, a $\sim 50\%$ change in the difference in the hole effective g-factors of two coupled QDs forming a singlet-triplet qubit on adjustment of the inter-dot coupling is demonstrated.

ACKNOWLEDGMENTS

We thank Motoi Takahashi for valuable contributions to this work. This work was performed, in part, at the Center for Integrated Nanotechnologies, a U.S. DOE, Office of Basic Energy Sciences, user facility. Sandia National Laboratories is a multi-mission laboratory managed and operated by National Technology and Engineering Solutions of Sandia, LLC., a wholly owned sub-

subsidiary of Honeywell International, Inc., for the U.S. Department of Energy's National Nuclear Security Administration under contract DE-NA-0003525. The view ex-

pressed in the article do not necessarily represent the views of the U.S. Department of Energy or the United States Government.

-
- [1] S. Studenikin, M. Korkusinski, A. Bogan, L. Gaudreau, D. G. Austing, A. S. Sachrajda, L. Tracy, J. Reno, and T. Hargett, *Semicond. Sci. Technol.* **36**, 053001 (2021).
- [2] C. Flindt, A. S. Sørensen, and K. Flensberg, *Phys. Rev. Lett.* **97**, 240501 (2006).
- [3] D. V. Bulaevand D. Loss, *Phys. Rev. Lett.* **98**, 097202 (2007).
- [4] P. Szumniak, S. Bednarek, B. Partoens, and F. M. Peeters, *Phys. Rev. Lett.* **109**, 107201 (2012).
- [5] P. Szumniak, S. Bednarek, J. Pawłowski, and B. Partoens, *Phys. Rev. B* **87**, 195307 (2013).
- [6] B. Venitucciand Y.-M. Niquet, *Phys. Rev. B* **99**, 115317 (2019).
- [7] A. Bogan, S. Studenikin, M. Korkusinski, L. Gaudreau, P. Zawadzki, A. S. Sachrajda, L. Tracy, J. Reno, and T. Hargett, *Phys. Rev. Lett.* **120**, 207701 (2018).
- [8] S. Studenikin, M. Korkusinski, M. Takahashi, J. Ducatel, A. Padawer-Blatt, A. Bogan, D. G. Austing, L. Gaudreau, P. Zawadzki, A. Sachrajda, *et al.*, *Commun. Phys.* **2** (2019).
- [9] V. N. Golovach, M. Borhani, and D. Loss, *Phys. Rev. B* **74**, 165319 (2006).
- [10] E. I. Rashba, *Phys. Rev. B* **78**, 195302 (2008).
- [11] K. C. Nowack, F. H. L. Koppens, Y. V. Nazarov, and L. M. K. Vandersypen, *Science* **318**, 1430 (2007).
- [12] N. Hendrickx, D. Franke, A. Sammak, G. Scappucci, and M. Veldhorst, *Nature* **577**, 487 (2020).
- [13] F. Froning, L. Camenzind, O. van der Molen, A. Li, E. Bakkers, D. Zumbühl, and F. Braakman, *Nature Nanotechnology* **16**, 308 (2021).
- [14] A. Bogan, S. A. Studenikin, M. Korkusinski, G. C. Aers, L. Gaudreau, P. Zawadzki, A. S. Sachrajda, L. A. Tracy, J. L. Reno, and T. W. Hargett, *Phys. Rev. Lett.* **118**, 167701 (2017).
- [15] L. A. Tracy, T. W. Hargett, and J. L. Reno, *Appl. Phys. Lett.* **104**, 123101 (2014).
- [16] L. A. Tracy, J. L. Reno, and T. W. Hargett, Sandia Report SAND2015-8132 (2015).
- [17] A. Bogan, S. Studenikin, M. Korkusinski, L. Gaudreau, P. Zawadzki, A. Sachrajda, L. Tracy, J. Reno, and T. Hargett, *Commun. Phys.* **2** (2019).
- [18] See Supplemental Material at <http://link...> for figures showing Fig. 1(c) plotted over a wider gate voltage range with the charge boundaries and hole occupation numbers included, and g_R^* as a function of magnetic field for SC and WC1 inter-dot coupling conditions.
- [19] J. Ducatel, A. Padawer-Blatt, A. Bogan, M. Korkusinski, P. Zawadzki, A. Sachrajda, S. Studenikin, L. Tracy, J. Reno, and T. Hargett, *Appl. Phys. Lett.* **118**, 214002 (2021).
- [20] T. A. Baart, M. Shafiei, T. Fujita, C. Reichl, W. Wegscheider, and L. M. K. Vandersypen, *Nature Nanotechnology* **11**, 330 (2016).
- [21] T. A. Baart, T. Fujita, C. Reichl, W. Wegscheider, and L. M. K. Vandersypen, *Nature Nanotechnology* **12**, 26 (2017).
- [22] T. Fujita, T. A. Baart, C. Reichl, W. Wegscheider, and L. M. K. Vandersypen, *npj Quantum Information* **3** (2017).
- [23] V. P. Michal, T. Fujita, T. A. Baart, J. Danon, C. Reichl, W. Wegscheider, L. M. K. Vandersypen, and Y. V. Nazarov, *Phys. Rev. B* **97**, 035301 (2018).
- [24] D. Jirovec, A. Hofmann, A. Ballabio, P. M. Mütter, G. Tavani, M. Botifoll, A. Crippa, J. Kukucka, O. Sagi, F. Martins, *et al.*, *Nature Materials* **20**, 1106 (2021).
- [25] A. V. Nenashev, A. V. Dvurechenskii, and A. F. Zinovieva, *Phys. Rev. B* **67**, 205301 (2003).
- [26] M. Korkusinskiand P. Hawrylak, *Phys. Rev. B* **87**, 115310 (2013).
- [27] S. Amasha, K. MacLean, I. P. Radu, D. M. Zumbühl, M. A. Kastner, M. P. Hanson, and A. C. Gossard, *Phys. Rev. Lett.* **100**, 046803 (2008).
- [28] L. C. Camenzind, L. Yu, P. Stano, J. D. Zimmerman, A. C. Gossard, D. Loss, and D. M. Zumbühl, *Nat. Commun.* **9**, 3454 (2018).
- [29] J. H. Prectel, F. Maier, J. Houel, A. V. Kuhlmann, A. Ludwig, A. D. Wieck, D. Loss, and R. J. Warburton, *Phys. Rev. B* **91**, 165304 (2015).
- [30] Z. Wasilewski, S. Fafard, and J. McCaffrey, *Journal of Crystal Growth* **201-202**, 1131 (1999).
- [31] M. Pioro-Ladrière, T. Obata, Y. Tokura, Y.-S. Shin, T. Kubo, K. Yoshida, T. Taniyama, and S. Tarucha, *Nat. Phys.* **4**, 776 (2008).
- [32] C. Kloeffer, M. Trif, P. Stano, and D. Loss, *Phys. Rev. B* **88**, 241405(R) (2013).
- [33] M. Veldhorst, C. H. Yang, J. C. C. Hwang, W. Huang, J. P. Dehollain, J. T. Muhonen, S. Simmons, A. Laucht, F. E. Hudson, K. M. Itoh, *et al.*, *Nature* **526**, 410 (2015).
- [34] T. F. Watson, S. G. J. Phillips, E. Kawakami, D. R. Ward, P. Scarlino, M. Veldhorst, D. E. Savage, M. G. Lagally, M. Friesen, S. N. Coppersmith, *et al.*, *Nature* **555**, 633 (2018).
- [35] X. Mi, J. V. Cady, D. M. Zajac, P. W. Deelman, and J. R. Petta, *Science* **355**, 156 (2017).
- [36] Y. Li, S.-X. Li, F. Gao, H.-O. Li, G. Xu, K. Wang, D. Liu, G. Cao, M. Xiao, T. Wang, *et al.*, *Nano Lett.* **18**, 2091 (2018).
- [37] R. Wang, R. S. Deacon, J. Sun, J. Yao, C. M. Lieber, and K. Ishibashi, *Nano Lett.* **19**, 1052 (2019).
- [38] F. Borjans, X. G. Croot, X. Mi, M. J. Gullans, and J. R. Petta, *Nature* **577**, 195 (2020).
- [39] L. Gaudreau, A. Bogan, M. Korkusinski, S. Studenikin, D. G. Austing, and A. S. Sachrajda, *Semicond. Sci. Technol.* **32**, 093001 (2017).